

Diaphragm border detection in coronary X-Ray angiographies: new method and applications

Simeon Petkov, Xavier Carrillo Suarez, Petia Radeva and Carlo Gatta

Abstract

X-ray angiography is widely used in cardiac disease diagnosis. The diaphragm motion induces gray-level changes, which are one of the main obstacles in quantitative analysis of myocardial perfusion. In this paper we focus on detecting the diaphragm border in coronary X-ray angiographies. The proposed method outperforms state of the art approaches. We extend a previous publicly available data set, adding new ground truth data. Finally, we show three applications of our method: (1) a strategy to reduce false positives in vessel enhanced images; (2) a digital diaphragm removal algorithm; (3) an improvement in Myocardial Blush Grade semi-automatic estimation.

Index Terms

X-ray, angiography, diaphragm, myocardial blush grade, DSA, vesselness

I. INTRODUCTION

In diseases related to heart malfunctioning, it is important to ensure proper blood supply to the heart and estimate the healthiness of the myocardial tissue. For this purpose, medical doctors insert a catheter into the affected coronary artery and inject a radio-opaque liquid through it. The liquid flows through the arteries and perfuses the myocardium. This process is recorded as an angiography video sequence using X-ray technology. Figure 1 shows an exemplar angiographic image. The arteries are clearly visible as they are filled with the contrast liquid. The diaphragm is also visible as a darkened area due to the fact that it is a thick muscle. Usually, other structures like bones or gas are visible as bright or dark areas with varying gray level intensity and strength of the contours that delineate them. When contrast liquid perfuses myocardium, it is seen as a gray staining, which is brighter than arteries and diaphragm. The

motion of the diaphragm follows the patient's breathing pattern; since the diaphragm often overlaps with the myocardium, it complicates both visual and automatic inspection of the myocardial perfusion.

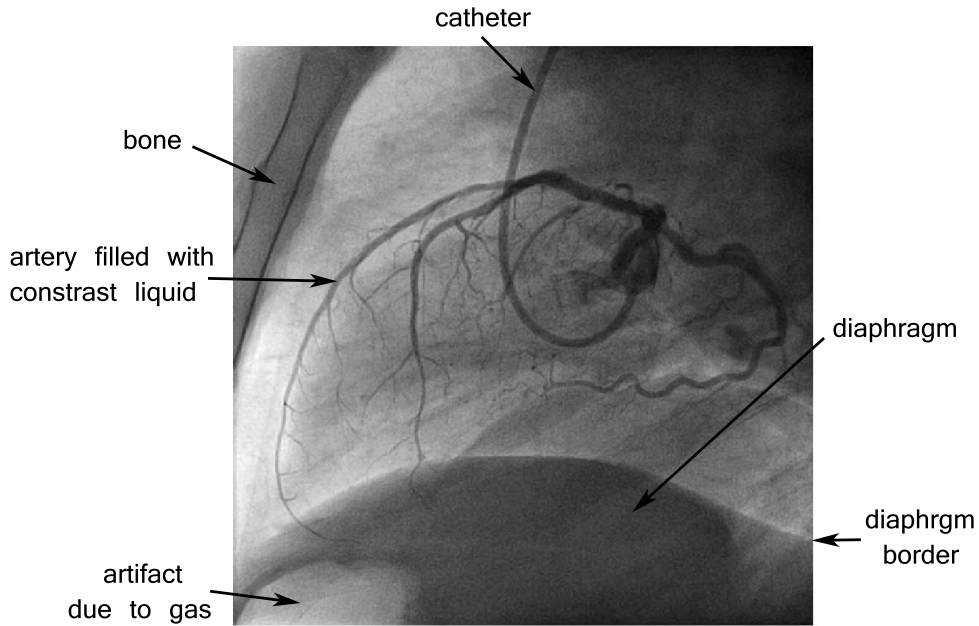


Figure 1. An exemplar frame from a coronary angiography sequence.

A. Motivation

An automatic method detecting the diaphragm border would be useful on two levels: (1) to digitally remove the diaphragm from X-ray angiographies and (2) to improve existing algorithms for analysis of myocardial perfusion. Digital removal of the diaphragm could help medical doctors when visually estimating myocardium healthiness. Additionally, several automatic or semi-automatic methods for myocardial perfusion estimation have been proposed in the last seven years [1], [2], [3], [4]; all of them are negatively affected by the diaphragm motion. In [1] authors make explicit use of a method for diaphragm border detection [5] to improve the quality of the region-of-interest tracking that is used to measure the myocardial perfusion. In [3], authors claim that the breathing movements can hide staining patterns, showing that the diaphragm movement and the consequent gray-level variation in an area can reduce the method ability to measure the myocardial staining. In [4], authors impose the angiography sequence

1
2
3
4 acquisition to be done while the patient holds breath and show that the diaphragm movement introduces
5 artifacts in the resulting analysis. It has to be noted that not all patients can hold breath for the time
6 required to record a complete sequence for myocardial perfusion analysis, i.e. at least 7 seconds. In the
7 preliminary work in [2], authors claim that one limitation of their method is that the manually delineated
8 perfusion area must be isolated from the diaphragm, so that the method applicability is reduced for
9 certain angiographic projections. All these methods can benefit of a pre-processing step able to detect
10 the diaphragm border. Section V-C shows how a digital diaphragm removal improves the method in [3].

11
12
13
14
15
16
17 Another method that can make use of a diaphragm detection is the vesselness filter in [6]. It often
18 detects the diaphragm border as a false positive vessel. Section V-A describes an algorithm to remove
19 false positive vessels, based on diaphragm detection method.
20
21
22

23 *B. State of the art*

24
25
26 To the best of our knowledge, two methods for automatic diaphragm detection in cardiac X-ray
27 angiographies have been proposed so far in [5] and [7]. In [5], authors model the diaphragm as an
28 arc of a circle. A pre-processing step removes narrow contrast objects like arteries and the catheter by
29 means of morphological closing operator. Then, a Canny edge detector defines an edgeness map for the
30 pre-processed image. For any arc in the image plane, authors assign a score - the sum of the edgeness
31 values of the pixels composing the arc. The circle that maximizes that score is the optimal prediction. The
32 initial result is refined with active contours (a.k.a. snakes) if a confidence measure indicates that it is not
33 good enough. In [7], authors adopt a similar approach as in [5] to remove arteries and highlight edges.
34 Then, a set of paths is constructed by tracking edges from one frame to the next. K-means clustering
35 divides the paths in three clusters. The method keeps only the paths that follow the breathing pattern by
36 selecting the cluster of highest quality paths as defined in [7], Section 2.4. The geometric model for the
37 diaphragm border in [7] is a parabola; the final step of the method is to find the optimal parabola for
38 each frame by removing outlying paths.
39
40
41
42
43
44
45
46
47

48
49 The method in [7] has one main drawback - it cannot make a prediction for a single frame before
50 processing the whole sequence, while the method in [5] operates individually on each frame. Regarding
51 the computational efficiency, both of the methods do not achieve runtime performance due to the use
52 of extensive searches - [7] in the path constructing process and [5] when finding the optimal circle
53 parameters. The models used in the two methods show that none of them has the flexibility to represent
54 the diversity of diaphragm borders. The circle is too simple and extensive search over circular arcs often
55 leads to non-plausible detections. The parabola is not flexible enough either to model diaphragm border
56
57
58
59
60
61
62
63
64
65

curves, since it is symmetric along a single axis and this assumption is not true for all diaphragm borders.

Although the following two papers do not present an automatic diaphragm detection method, they are worth mentioning. In [8], a method to track anatomical curves in X-ray sequences is presented. The method requires manual initialization of the curve to be tracked and clearly outperforms a classical optical flow technique. In [9], authors present a method that estimates the "background" layer of an X-ray angiography sequence. The goal is to perform a form of digital subtraction in angiographies, which highlights coronary arteries. The method is based on a Bayesian framework, which combines tracking and modeling of the background. Prior to contrast liquid injection, it requires that a small number of images are acquired at different cardiac cycles and breathing phases to serve as static masks for the background estimation.

Our paper contributes with a new diaphragm border detection method that outperforms previous ones (Section IV). The proposed method is novel in making use of a-priori knowledge for the shape of the diaphragm border. This reduces the possibility of non-plausible predictions caused by edges that do not belong to the diaphragm border. We also provide a quantitative evaluation of different models for the diaphragm border (Section II-A). The methodology for digital diaphragm removal from X-ray angiographies (Section V-B) is another contribution. In addition, we extended the publicly available data set adding new images that increase the diversity of cases.

II. DIAPHRAGM BORDER DETECTION

Our method is composed by a training phase and three main steps, as depicted in Figure 2. The trained model introduces a probability criterion for the diaphragm border shape. In the first step of the method, a morphological pre-processing removes the arteries and the catheter. The second step computes an edgeness map by means of first order vertical derivatives within a Gaussian pyramid [10]. The last step estimates the optimal diaphragm border, maximizing two criteria - (1) the diaphragm border shape probability and (2) the normalized edgeness value collected by the pixels that belong to the border. The proposed method has three parameters:

- The size of the structuring disk for the morphological operator.
- The standard deviation of the normal probability distribution expressing the diaphragm border positional uncertainty.
- The regularization factor for the diaphragm shape probability.

Subsection II-A explains the rationale for using a polynomial curve to model the diaphragm border and following subsections explain in detail each of the method modules. The last Subsection II-F describes

the validation we performed for tuning the three method parameters.

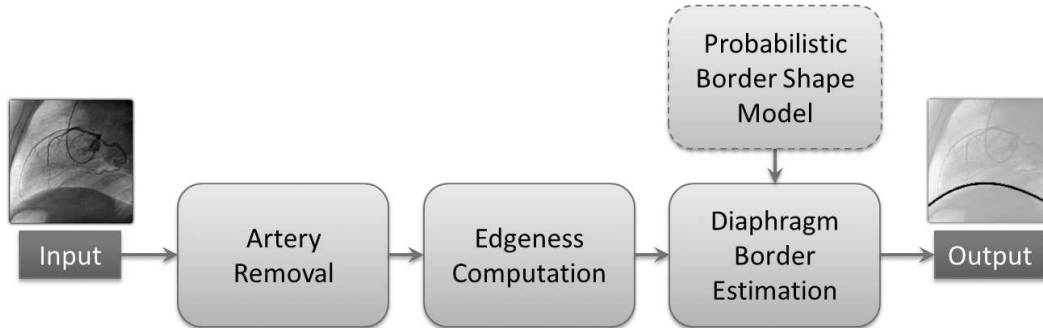


Figure 2. Block scheme of our method.

A. Evaluating different models for the diaphragm border

To compare different diaphragm border models, we fitted various choices to the annotated ground truth curves of data sets A and B (described in Section III). We evaluated quantitatively a circular model $R^2 = (x - x_c)^2 + (y - y_c)^2$ and polynomial curves of the form $y = \sum_{i=0}^N a_i x^i$, where $N \in \{2, 3, 4, 5, 6, 7\}$. Polynomials of 0th and 1st order are bad choices because the diaphragm border is physiologically not plausible to appear as a straight line.

Table I contains the quantitative results for each model. We used two error measures: the Mean Minimal Distance (d_{MMD}) and the Hausdorff Distance (d_{HD}). The Mean Minimal Distance gives information about the precision of the prediction while the Hausdorff Distance is an indicator of the robustness. Rigorous description of these measures is provided in Section IV. Numerical results indicate that the parabola is a better choice than the circle. The results for d_{MMD} and d_{HD} consistently improve as the polynomial degree increases. This is an indication that the potential of the polynomial model to represent the variety of diaphragm borders increases with its degree. Considering the results from Table I we use polynomial model for the diaphragm border.

B. Diaphragm border shape training

The variation in diaphragm shape is little with respect to different patients and projections. Considering this, we estimate the probability distribution of the diaphragm border shape over the model parameters,

	d_{HD}	d_{MMD}
	Avg±std	Avg±std
<i>circle</i>	27.22±53.42	4.80±11.02
<i>2nd degree polynomial</i>	17.80±12.02	3.24±1.66
<i>3rd degree polynomial</i>	10.70±8.04	2.04±1.11
<i>4th degree polynomial</i>	6.30±4.99	1.19±0.60
<i>5th degree polynomial</i>	4.79±3.50	0.96±0.45
<i>6th degree polynomial</i>	3.86±2.63	0.77±0.32
<i>7th degree polynomial</i>	3.23±2.01	0.66±0.26

Table I

QUANTITATIVE RESULTS WHEN FITTING DIFFERENT MODELS TO THE GROUND TRUTH. THE ERROR MEASURES USED FOR PERFORMANCE EVALUATION ARE DEFINED IN SECTION IV.

using Gaussian Mixture Models. As explained in Section II-E we start estimating the diaphragm border using the parabolic model $y = a_0 + a_1x + a_2x^2$. Parameter a_2 represents the broadness/narrowness of the parabola and whether it is concave or convex. The a_1 parameter affects the horizontal shift and the scaling of the parabola and a_0 specifies its vertical translation. We are interested in building a probabilistic model for the shape of the diaphragm regardless its vertical position, so we estimate the joint probability $p(a_1, a_2|\mathcal{D})$ using a two-dimensional Gaussian Mixture Model and the ground truth of a certain training data \mathcal{D} . Estimating the joint probability density for all the polynomial parameters except a_0 is still valid for $N > 2$, as a_0 specifies the vertical displacement of the curve, while the other parameters specify its shape.

C. Pre-processing: digital artery removal

When the arteries are filled with contrast liquid, they usually produce stronger edges than the diaphragm border. These edges could mislead our diaphragm detection, since it is based on edge analysis. We use a morphological closing operator to remove dark and thin structures. The structuring element of the operator is a disk and its radius is one of the parameters of our method. The effect of applying the morphological operator is shown in Figure 3; it removes arteries and preserves edges that resemble diaphragm borders. The resulting circular artifacts have lower contrast than the arteries which is enough to reduce the possibility of suboptimal diaphragm edge analysis.

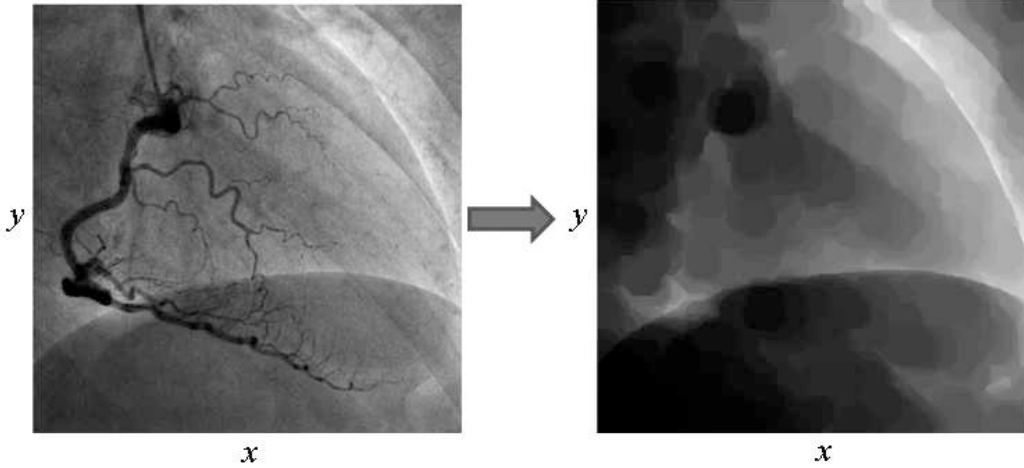


Figure 3. Morphological removal of dark and thin structures (right) on an X-ray image (left). The radius of the structuring disk for the operator is 27 pixels.

D. Edginess computation

To highlight consistent edges we compute an edginess map on the morphologically pre-processed image. First-order scale-space vertical derivative is applied as

$$D_{\sigma}(x, y) = \sigma I(x, y) * \frac{\partial G(y; 0, \sigma^2)}{\partial y}, \quad (1)$$

where $I(x, y) \in \mathbb{R}$ is the input image, $*$ denotes the convolution operator, $G(y; 0, \sigma^2)$ is a zero-mean Gaussian and σ is the scale parameter [11]. The set of scales for the derived Gaussians $\Phi = \{1, 2, 4, 8, 16\}$ is defined in octaves of pixels so that it covers all possible sizes of edges that could be produced by the diaphragm border. To make the results for different scales comparable, we apply the Lindeberg normalization [11], i.e. multiplication by the scale σ .

In all standard projections for recording X-Ray angiographies, the diaphragm is situated below the diaphragm border, so we modify the edge computation to nullify edges that correspond to lighter pixels below and darker pixels above:

$$\tilde{D}_{\sigma}(x, y) = \begin{cases} D_{\sigma}(x, y) & \text{if } D_{\sigma}(x, y) > 0 \\ 0 & \text{if } D_{\sigma}(x, y) \leq 0. \end{cases} \quad (2)$$

We combine the maps for all scales $\tilde{D}_{\sigma}(x, y)$ into a single map by averaging the values over the number of scales:

$$\tilde{E}(x, y) = \frac{1}{|\Phi|} \sum_{\sigma \in \Phi} \tilde{D}_{\sigma}(x, y). \quad (3)$$

Finally, to ensure the edgeness $E(x, y) \in [0, 1]$, we apply the following non-linear transformation:

$$E(x, y) = 1 - \exp(-\tilde{E}(x, y)). \quad (4)$$

Figure 4 shows an example of an edgeness map. The pixels with high edgeness values consistently delineate the two edges that look like a diaphragm border. The rest of the pixels with positive edgeness are scattered around the image and produce weaker signal than the edges resembling a diaphragm border.

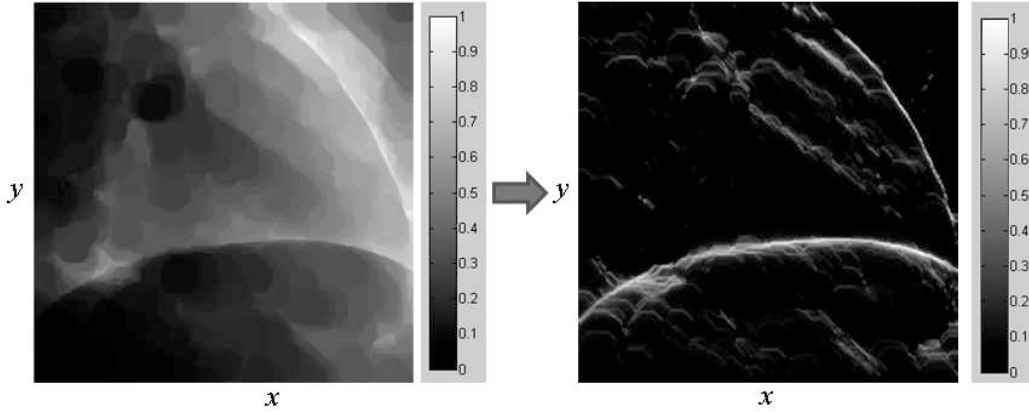


Figure 4. A morphologically pre-processed frame (left) and its Edgeness map (right).

E. Diaphragm border estimation

We estimate the values $\{\hat{a}_0, \dots, \hat{a}_N\}$ that define the optimal polynomial curve of N^{th} degree, which delineates the diaphragm border. Let X be the width and Y the height of a frame. We minimize the following cost function:

$$Q(a_0, \dots, a_N) = - \underbrace{\frac{1}{|\mathcal{R}|} \sum_{(x_r, y_r) \in \mathcal{R}} E(x_r, y_r)}_{\text{data}} - \xi \underbrace{p(a_1, \dots, a_N | \mathcal{D})}_{\text{a-priori shape}}, \quad (5)$$

where $\mathcal{R} = \{(x_r, \sum_{i=0}^N a_i x_r^i)\}$ for $x_r \in \{1, \dots, X\}$ is the set of pixels constructing a polynomial curve. To exclude points falling outside the image boundaries, if $y_r \notin [1, Y]$ for some x_r , the pair (x_r, y_r) is removed from \mathcal{R} . The data term represents the criterion for maximizing the average edgeness value for the pixels that belong to the curve. The a-priori shape term makes use of the a-priori knowledge about the diaphragm shape (Section II-B); it maximizes the joint probability for the polynomial parameters with

respect to the estimated joint probability density on a certain training data \mathcal{D} . The regularization factor for the diaphragm shape probability ξ is a parameter of our method. As it is shown in Figure 4, the edgeness map E is not precise in highlighting the diaphragm curve. We express the positional uncertainty using a normal probability distribution. This can be quickly implemented by applying a Gaussian filtering on the Edgeness map. The standard deviation of the Gaussian is another parameter of our method.

As stated in Section II-A, diaphragm border is not prone to appear as straight line. According to the results from Table I the parabola ($N = 2$) is the polynomial with the lowest order that achieves good balance between precision and robustness. We start estimating the diaphragm border with $N = 2$. To avoid falling into local minima when minimizing the cost function (5), we construct a set of M hypotheses drawn by the estimated probability densities for a_1 and a_2 . The bootstrapping for a_0 covers the range of vertical positions so that the parabolic curves fall into the frame spatial support. For initialization we select the triplet $\{a_0, a_1, a_2\}$ that maximizes the data term of the cost function (5). The minimization of the cost function (5), by means of standard gradient descent algorithm, estimates the optimal values \hat{a}_0 , \hat{a}_1 and \hat{a}_2 . To improve the precision of the detection, we iteratively increase the polynomial order N by one degree, initializing the parameter values to the estimated in the previous iteration. The new parameter a_N is initialized to zero. By minimizing the cost function (5) again, we find the polynomial curve of order N that models the diaphragm border. This iterative process can be repeated up to the desired order.

In [12, Chapter 1, page 7] C. Bishop shows how increasing the order of a polynomial model also increases the possibility of overfitting the data. The results in Figure 5 confirm the negative effect if we try to estimate the diaphragm border curve directly with $N \geq 3$.

F. Parameters tuning

As Section II specifies, our method has three parameters that require initialization. Prior to testing we estimate their optimal values with an extensive search that optimizes method performance on validation data. Section III describes the data sets and Section IV explains how they are being distributed between training, validation and testing. The mean and the standard deviation of the estimated values for the method parameters are listed in Table II. The tuning process considered zero as an optional value for each parameter. Setting a parameter to zero is equivalent to omit the corresponding step. Zero was never estimated as optimal value for none of the parameters. This observation shows the need of morphological pre-processing, positional uncertainty modeling and a-priori knowledge in our method.

Method parameter	mean±std of estimated values
Radius of the structuring disk for the morphological operator	27.47±1.45
Standard deviation of the positional uncertainty	6.92±1.32
Regularization factor for the diaphragm shape probability	0.015±0.013

Table II

THE MEAN AND THE STANDARD DEVIATION OF THE ESTIMATED VALUES FOR THE METHOD PARAMETERS.

III. MATERIAL

We used the publicly available set proposed in [7] (a.k.a. data set A). To increase its diversity, we extended it with additional 58 frames (from 30 patients) for a total of 74 frames (from 41 patients)¹. We also composed another set of frames - data set B². It contains 36 frames (from 18 patients). In some images from data set B it is hard to delineate the diaphragm precisely even for specialists; the border is not clearly visible and it does not touch the borders of the image plane. In other images the diaphragm border is well seen but it has peculiar shape. Considering these observations, dividing the whole data into two sets will provide interesting insights during testing.

To compute the inter-observer variability, the ground truth for all additional frames was annotated independently by two experts. Angiography sequences have been acquired using is a Philips Allura Xper FD20. The average pixel resolution has been estimated to be 0.34×0.34 mm. The C-arm's primary and secondary angles in data set A vary from -41° to 97° and from -17° to 33° respectively. For data set B the primary and secondary angles vary from -43° to 92° and from -16° to 28° .

IV. EVALUATION

We used the evaluation protocol proposed in [7], which is based on curve-to-curve distance errors. It is composed of two error measures: the Mean Minimal Distance (d_{MMD}) and the Hausdorff Distance (d_{HD}). The definition of d_{MMD} measure is:

$$d_{MMD}(P, GT) = \frac{1}{|P|} \sum_{i \in P} \min_{j \in GT} d(i, j), \quad (6)$$

¹Data set A is available at <https://sites.google.com/site/diaphragmdetection/engineering-docs>

²Data set B is available at <https://sites.google.com/site/diaphragmdetection/engineering-docs/validation-set-b>

where P is the set of all points from the predicted diaphragm curve, GT is the set of all points from the ground truth curve and $d(i, j)$ is the Euclidean distance between two points i and j . The definition of d_{HD} is:

$$d_{HD}(P, GT) = \max\left\{\sup_{i \in P} \inf_{j \in GT} d(i, j), \sup_{j \in GT} \inf_{i \in P} d(i, j)\right\}, \quad (7)$$

which is the Euclidean distance between the two most remote points from each of the sets. It has to be noted that while d_{HD} is symmetric, d_{MMD} is not. The rationale for combining two error measures is based on the conclusion from [7] that each of the measures represents different performance aspects. The measure d_{HD} is very sensitive to predicted points laying far from the ground truth points. However, it gives little information about the overall precision of the prediction. This makes it useful for measuring robustness. The other measure, d_{MMD} , is an indicator of the average precision of the prediction.

We followed the LOPO (Leave-One Patient Out) cross-validation technique, in which we split the data in two parts. Images for one patient are used for testing, half of the remaining images to train the probabilistic model, and the rest for tuning the optimal values for the method parameters. The process is repeated so that the data for each patient is used only once for testing.

Tables III and IV show the quantitative results respectively on data set A and B. The method in [5]

	d_{HD}			d_{MMD}		
	Avg±Std	min	max	Avg±Std	min	max
$O1$ vs $O2$	19.64±27.90	3.16	183.17	2.77±6.06	0.77	52.39
$O2$ vs $O1$	19.64±27.90	3.16	183.17	1.73±1.75	0.71	15.65
[5]	81.88±102.53	18.03	482.15	33.28±45.06	5.10	236.24
[5] (with snakes)	82.11±97.18	16.40	468.00	26.08±43.81	3.84	237.66
[7]	107.03±102.80	5.39	378.08	34.74±43.69	1.28	168.31
Our (N=2)	48.76±57.29	7.58	518.88	9.86±18.67	2.50	164.51
Our (N=3)	47.87±57.68	8.10	518.93	9.40±18.74	2.40	164.58
Our (N=4)	47.64±57.78	8.13	518.94	9.35±18.76	2.35	164.60
Our (N=5)	48.39±58.01	7.41	519.20	10.02±18.35	2.27	161.17
Our (N=6)	49.32±58.15	9.29	519.20	10.28±18.32	2.37	161.16
Our (N=7)	49.32±58.15	9.29	519.20	10.31±18.32	2.37	161.16

Table III

QUANTITATIVE RESULTS ON DATA SET A. ALL MEASURES ARE IN PIXELS.

	d_{HD}			d_{MMD}		
	Avg±Std	min	max	Avg±Std	min	max
$O1$ vs $O2$	38.98±63.19	3.16	378.19	2.45±2.69	0.82	16.85
$O2$ vs $O1$	38.98±63.19	3.16	378.19	4.48±13.65	0.74	83.59
[5]	137.18±130.33	21.95	520.03	45.48±60.26	13.71	288.44
[5] (with snakes)	115.39±122.20	17.03	518.99	39.83±71.01	10.43	350.07
[7]	170.75±81.21	21.47	425.88	53.75±51.03	3.38	221.60
Our (N=2)	102.51±62.80	23.93	377.98	21.46±16.04	4.62	105.19
Our (N=3)	101.21±64.18	20.00	377.98	20.41±16.57	4.23	105.19
Our (N=4)	101.00±64.30	20.00	377.97	20.32±16.60	4.18	105.19
Our (N=5)	99.96±64.06	23.33	377.97	20.00±16.57	3.81	105.19
Our (N=6)	100.04±64.31	20.00	377.97	20.35±16.75	4.27	105.19
Our (N=7)	100.04±64.32	20.00	377.97	20.49±16.59	3.92	105.19

Table IV
QUANTITATIVE RESULTS ON DATA SET B. ALL MEASURES ARE IN PIXELS.

clearly performs better than the method in [7] for both data sets. The performance of the method in [7] on data set A decreases compared to the evaluation performed in [7]; this indicates that the method does not generalize well on new images. Even with the lowest degree polynomial model, our method achieves better performance than both [5] and [7]. If we iteratively increase the polynomial degree from the 2nd to the 3rd the quantitative results improve on both data sets; The improvement continues for data set B when increasing the order of the polynomial to the 5th, while for data set A there is no improvement. Degrees higher than 5th result in slight performance degradation. The positive effect of iteratively increasing the polynomial model degree is more evident on the difficult cases in data set B; for the cases in validation set A the optimal degrees for the model are the 3rd and the 4rd.

Figure 5 plots d_{MMD} on the accumulated data from data sets A and B for two testing scenarios. Solid line is the d_{MMD} if the degree of the polynomial model is iteratively increased and the dashed line is the d_{MMD} if the method estimates the diaphragm border using directly higher than the second polynomial degree. The plot clearly shows the advantage of iteratively incrementing the flexibility of the model.

Figure 6 shows four visual results of our prediction, together with the predictions of [7], [5] and the ground truth. Examples (a) and (b) are from data set A and show that our method performs better than the state of the art. Examples (c) and (d) show cases from data set B, in which the diaphragm border

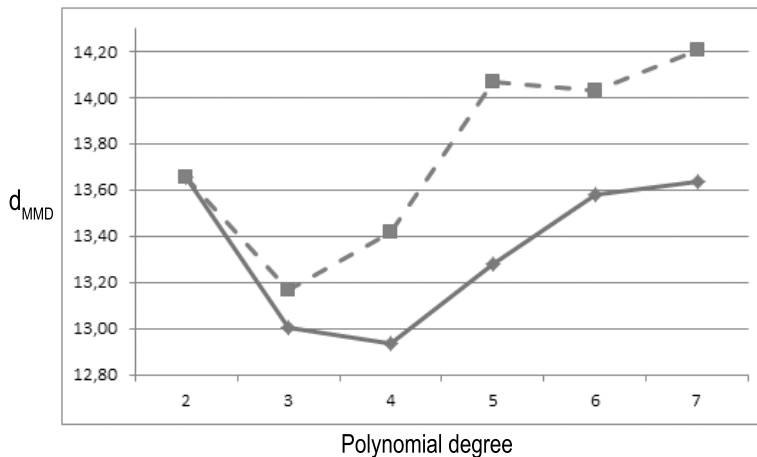


Figure 5. Plot of d_{MMD} on the accumulated data from data sets A and B for two testing scenarios. Solid line is the d_{MMD} if the degree of the polynomial model is iteratively increased and the dashed line is the d_{MMD} if the method estimates the diaphragm border using directly higher than the second polynomial degree.

does not touch the image plane borders. In examples (c) and (d) the predictions of both methods are suboptimal; in addition to the bad detection of the diaphragm border curves, their starting and ending points are not determined properly.

V. APPLICATIONS OF THE METHOD

As stated in Subsection I-A, the proposed method could improve other algorithms for coronary angiography processing. We provide three examples:

- (1) Removal of artifacts caused by the diaphragm border.
- (2) Digital diaphragm removal from X-ray angiographies.
- (3) Improvement of the semi-automatic Myocardial Blush estimation in [3].

A. Vesselness filter improvement

The vessel enhancement filter in [6] often detects the diaphragm edge as a false positive vessel. Figure 7(b) shows the filter output for the frame in Figure 7(a). We used the diaphragm border detection method to postprocess the vesselness map. Let $V(x, y)$ be the vesselness value for pixel (x, y) and Ω is the area that spans 15 pixels above and below the predicted diaphragm border. We attenuated the vesselness for each pixel in Ω as following:

$$\tilde{V}(x, y) = V(x, y) A(x, y) \mid (x, y) \in \Omega, \quad (8)$$

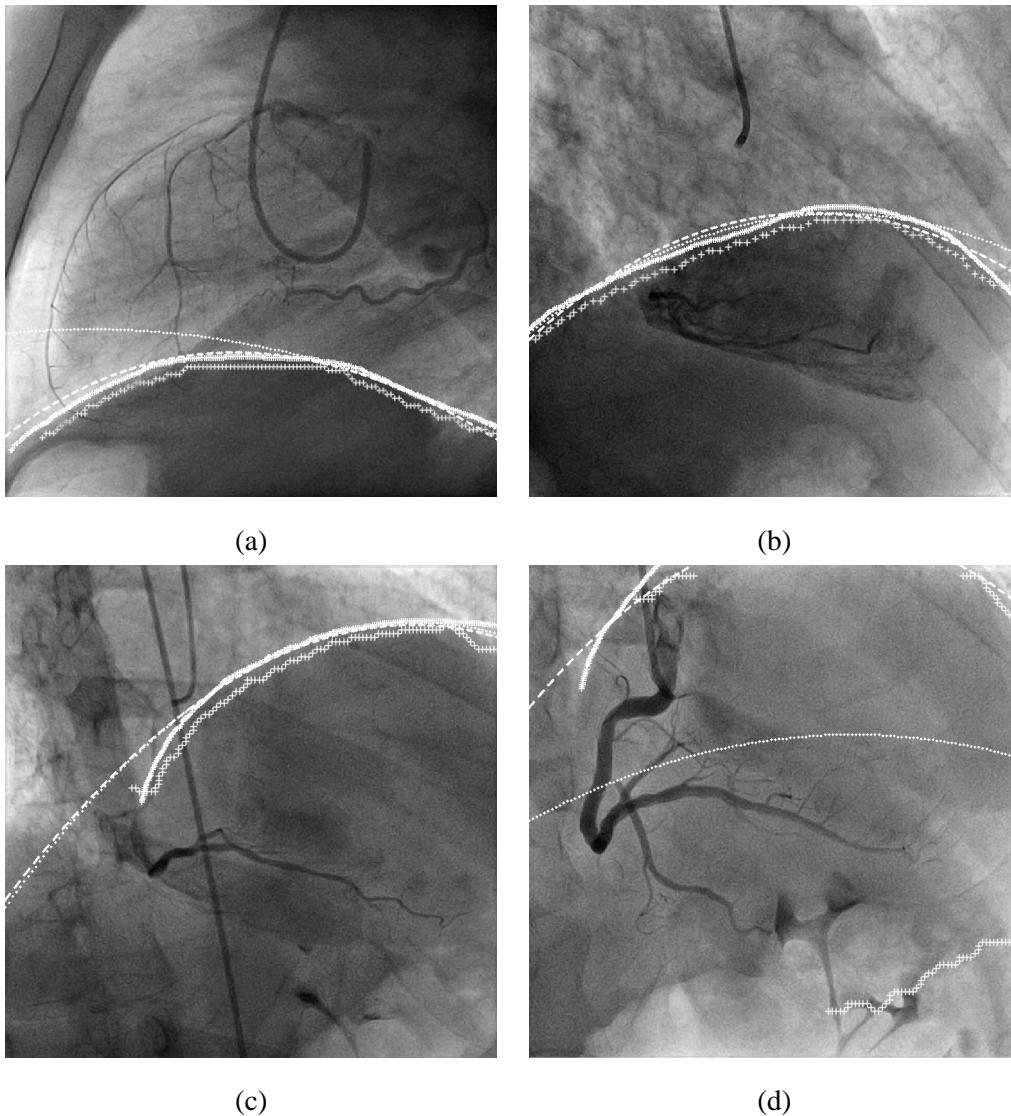


Figure 6. Visual results of our prediction together with the predictions of state of the art and manually annotated ground truth. Examples (a) and (b) are from the data set A and (c) and (d) are from data set B. The dashed line is our prediction, the dotted line is the prediction of [7], the '+' signs represent the prediction of [5] and the thick solid line is the ground truth marked by one of the specialists.

where the attenuation factor is:

$$A(x, y) = |\sin(\angle(\vec{r}_p, \vec{r}_v))|. \quad (9)$$

Here $\vec{r}_p \triangleq \vec{r}_p(x, \sum_{i=0}^N \hat{a}_i x^i)$ is the tangent vector to the diaphragm border and $\vec{r}_v \triangleq \vec{r}_v(x, y)$ is the orientation of the tubular structure at pixel (x, y) . To compute \vec{r}_p and \vec{r}_v we used first order derivative and Hessian matrix, respectively. Considering that $A \in [0, 1]$, if $V(x, y)$ is small before the improvement,

it will remain small after the improvement. This is sufficient to prevent introducing any artifact. If the two vectors \vec{r}_p and \vec{r}_v are perpendicular (meaning that a vessel is crossing the diaphragm border), then the vesselness value will stay the same. If the two vectors are parallel (an indication that a false positive detection is highly probable), the vesselness will become zero. Figure 7(c) shows the improvement in the vesselness map from Figure 7(b). It can be seen that the false positives caused by the diaphragm are almost completely removed while the vessels are preserved. Improving the general robustness of the vesselness filter from [6] is out of the scope of this paper - our goal here is to show how a simple algorithm, based on diaphragm detection, improves the result of the filter.

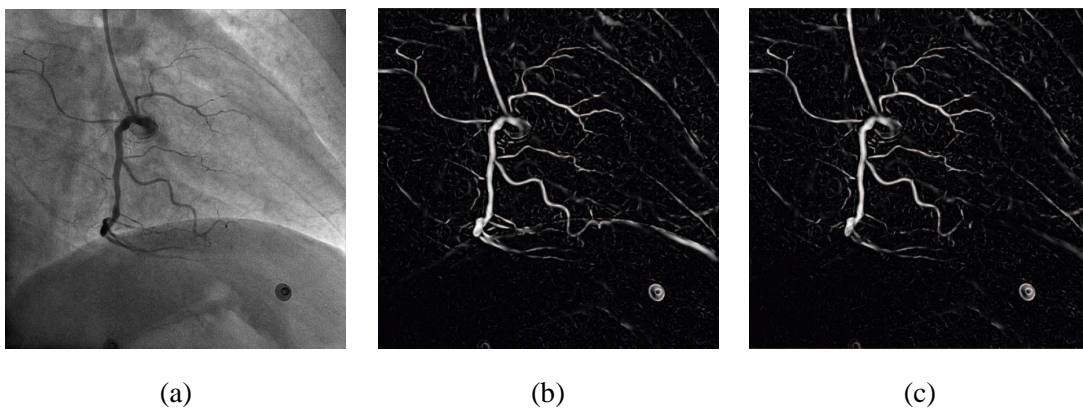


Figure 7. The effect of improving a vesselness map using our diaphragm prediction; (a) is the original frame, (b) is the vesselness map after applying the filter from [6] and (c) is the improved result after the postprocessing.

B. Digital Diaphragm Removal

In our algorithm for digital diaphragm removal, we look at an angiography as a volume $S(x, y, t) \in \mathbb{R}$, which has a compact support $\Theta = [1 X] \times [1 Y] \times [1 T] \subset \mathbb{N}^3$. X , Y and T are the size of the angiography in each dimension. Let $\Upsilon \subset \Theta$ be the subset of pixels below or on the diaphragm border and $\bar{\Upsilon} = \Theta \setminus \Upsilon$. We calculate the average gray values for Υ and $\bar{\Upsilon}$, respectively G_{Υ} and $G_{\bar{\Upsilon}}$. Considering the fact that the X-ray technology is multiplicative when displaying two overlapping objects [13], the proportion:

$$\rho = \frac{G_{\Upsilon}}{G_{\bar{\Upsilon}}} \quad (10)$$

gives the factor by which the diaphragm introduces darkening. We use ρ to digitally remove the darkening from the part of the volume that contains the diaphragm as:

$$\hat{S}(x, y, t) = \begin{cases} S(x, y, t), & \text{if } (x, y, t) \in \bar{\Upsilon} \\ S(x, y, t) \rho, & \text{if } (x, y, t) \in \Upsilon. \end{cases} \quad (11)$$

Figure 8 shows the effect of digital diaphragm removal on four cases; the first row contains the original images and the second row contains the images after the diaphragm has been digitally removed. Eliminating the darkening effect improves myocardial perfusion visibility. The diaphragm border detection is not perfect (equivalent to $d_{HD} = 0$), which results in dark gray and bright white artifacts.

Digital Subtraction Angiography is a well-known method to highlight arteries [14]. The third row shows the result of applying DSA to the original image. The darkness of the arteries is preserved while the background has lower gray intensity. The fourth row shows how the visualization of arteries improves when we apply DSA on the images after digitally removing the diaphragm.

C. Myocardial Blush Grade estimation improvement

Myocardial Blush Grade (MBG) is a subjective score for evaluating different levels of myocardial perfusion [15]. In X-ray videos the perfusion of contrast liquid is seen as gray staining. In [3], authors propose four descriptors of the myocardial staining pattern. The diaphragm movement affects negatively the performance of the method if the range covered by the diaphragm border overlaps with the myocardial tissue; hence we chose an X-ray angiography in which the diaphragm and the myocardium partially overlap. Fig 9(a) shows the map for the staining space descriptor generated by the method in [3]. Fig 9(b) depicts the same descriptor if we remove the diaphragm prior to MBG analysis. The difference in the visual results shows the improvement if the diaphragm is digitally removed; most of the artifacts caused by the breathing motion are removed while at the same time the myocardial perfusion is retained. Since the prediction is not precise at pixel level, not all artifacts related to the diaphragm are removed.

Figure 10 shows two plots of gray level variation through an entire angiography for a fixed region of the myocardium with size 15×15 pixels. Plot (a) is the gray level variation before the digital diaphragm removal and plot (b) shows the same information after it. The plot on the left shows that the patient inhales and exhales three times during the angiography. Each breathing cycle is visible as a peak to bright gray level which represents the inhaling while the diaphragm goes down. Then a drop-down to dark gray

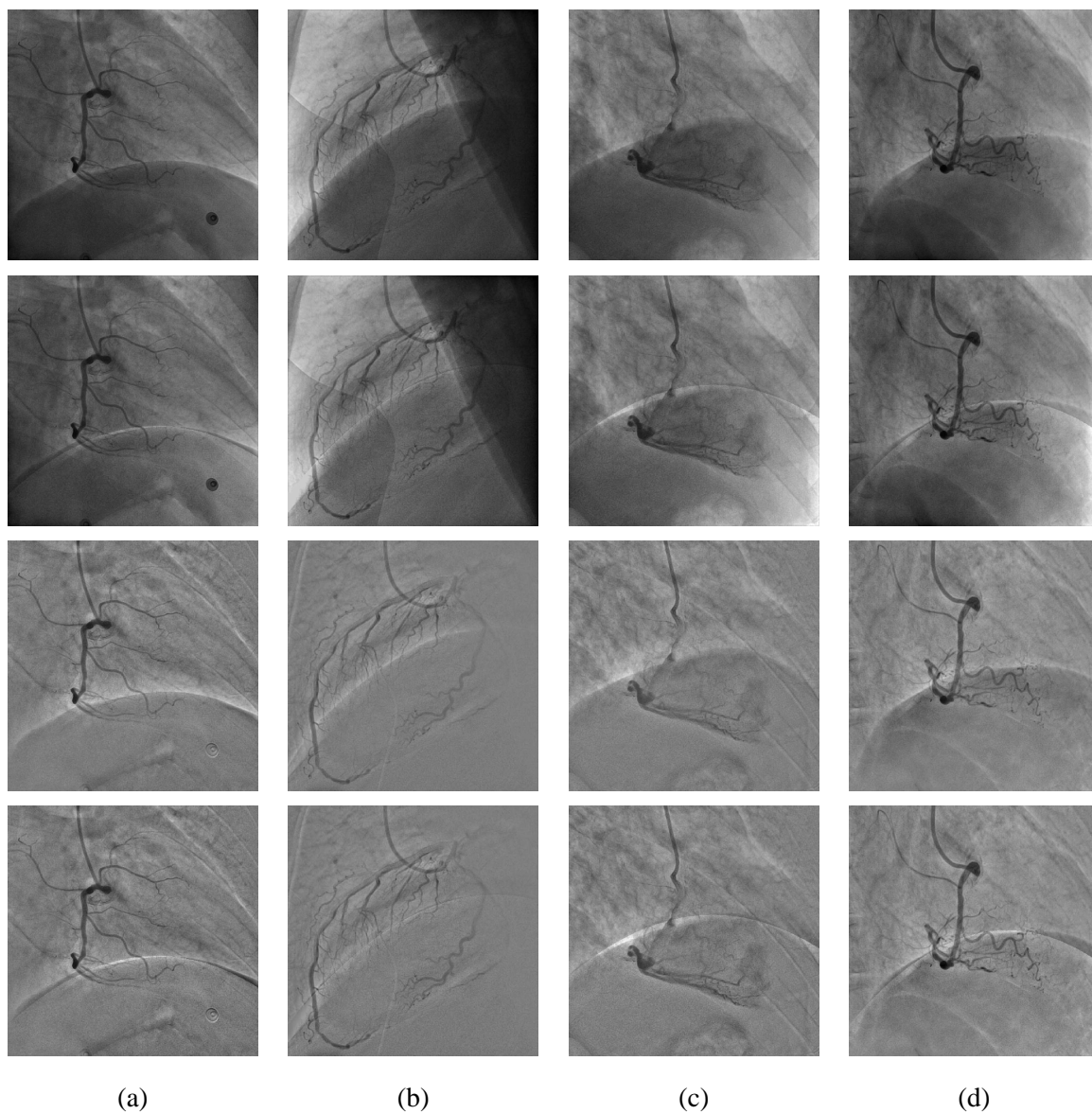


Figure 8. The effect of digital diaphragm removal on four cases. The first row contains the original images and the second row contains the images after the diaphragm has been removed. The third row shows the result of applying DSA to the original image. The fourth row demonstrates how the visualization of arteries improves when we apply DSA on the original image after removing the diaphragm from it.

level follows, representing the exhaling while the diaphragm goes up and covers the region. In the plot on the right the gray level variations due to the diaphragm have been drastically reduced.

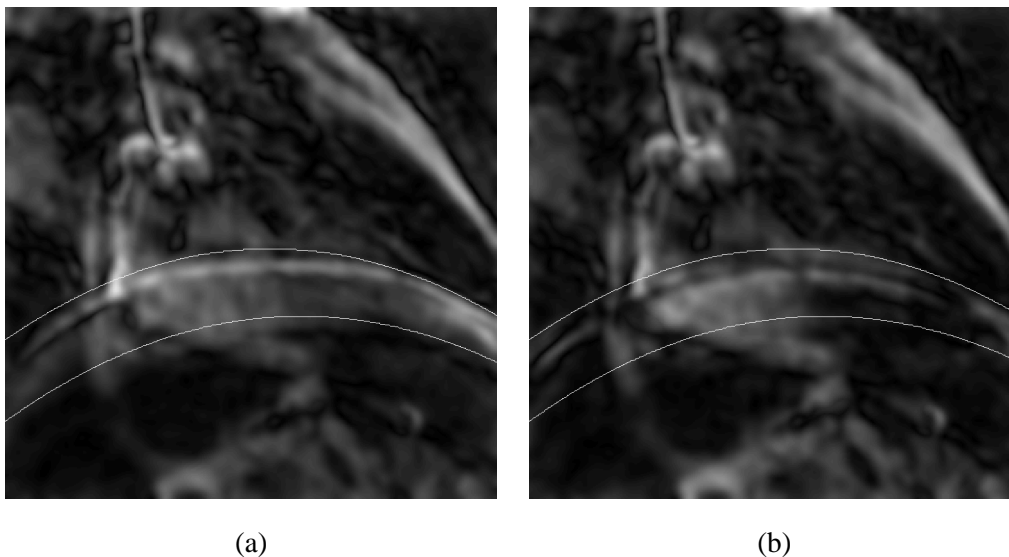


Figure 9. Improvement of the staining space descriptor in [3]; (a) depicts the staining space descriptor for an angiography sequence; (b) depicts the same descriptor after the diaphragm has been digitally removed. The range in which the diaphragm border moves is delineated with white lines. The whiter the pixel, the higher is the staining in the area.

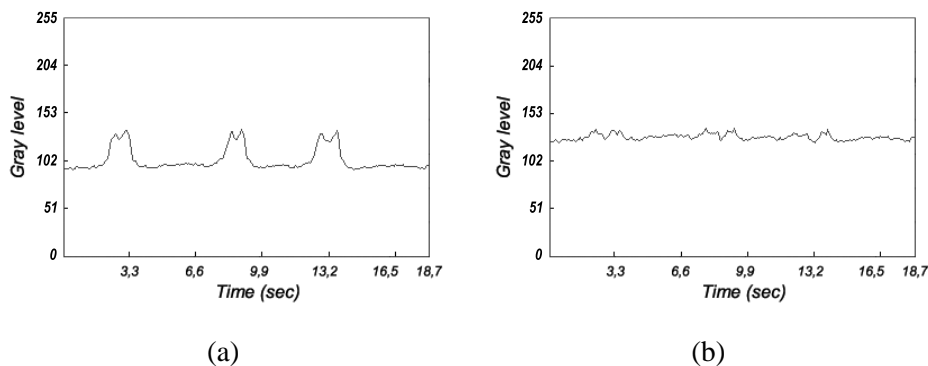


Figure 10. Two plots of the gray level variation through the whole angiography in a fixed region of the myocardium with size 15×15 pixels. Plot (a) is the gray level before the diaphragm removal and plot (b) shows the same information after the diaphragm has been removed.

VI. CONCLUSION

We proposed an automatic method to delineate the diaphragm border in X-ray angiography images and showed three applications of it: (1) digital removal of the diaphragm from X-ray angiographies, (2) improvement of the vesselness filter from [6] and (3) an improvement of the method for semi-automatic myocardial blush estimation from [3]. Our algorithm advances the state of the art, adopting a probabilistic

approach that requires much less computational cost than the path construction process in [7]. Iteratively increasing the flexibility of the polynomial model allows to improve the performance of our method.

However, two issues in automatic diaphragm detection remain unsolved: (1) Achieving errors that are close to the inter-observer variability. This requires precision on pixel level and a methodology to determine the starting and ending points of the diaphragm border; (2) Sometimes the diaphragm is seen as more than one distinct borders. So far, this has not been addressed. Such cases need to be considered when improving the state of the art in the field.

VII. CONFLICT OF INTEREST

- All authors have no evident conflict of interest, except for the obvious link with respective institutions.
- Some of the authors have been previously involved in a research program with Boston Scientific Corporation (BSC).
- Some of the authors still have academic and scientific discussions with BSC consultants and/or scientists.

VIII. ROLE OF THE FUNDING SOURCE

This work has been partially funded by the grant 2010 VALOR 00158, AGAUR. The work of S. Petkov is supported by AGAUR under an FI grant. The work of C. Gatta is supported by MICINN under a Ramon y Cajal Fellowship.

REFERENCES

- [1] A. Condurache, T. Aach, A. Kaiser, and P. Radke, “User-defined ROI tracking of the myocardial blush grade,” in *7th IEEE SSIAT*. Denver, CO: IEEE Computer Society, March 28-30 2006, pp. 66–70.
- [2] C. Gatta, J. D. G. Valencia, F. Ciompi, O. Rodriguez-Leor, and P. Radeva, “Toward robust myocardial blush grade estimation in contrast angiography,” in *IbPRIA*, 2009, pp. 249–256.
- [3] D. Gil, O. Rodriguez-Leor, P. Radeva, and J. Mauri, “Myocardial perfusion characterization from contrast angiography spectral distribution,” *IEEE TMI*, vol. 27, no. 5, pp. 641–649, 2008.
- [4] J. Liénard and R. Vaillant, “Quantitative tool for the assessment of myocardial perfusion during x-ray angiographic procedures,” in *Proceedings of the 5th ICFIMH*, ser. FIMH '09. Berlin, Heidelberg: Springer-Verlag, 2009, pp. 124–133.
- [5] A. Condurache, T. Aach, K. Eck, J. Bredno, and T. Stehle, “Fast and robust diaphragm detection and tracking in cardiac x-ray projection images,” in *Proc. SPIE*, 2005, pp. 1766–1775.
- [6] A. F. Frangi, W. J. Niessen, K. L. Vincken, and M. A. Viergever, “Multiscale vessel enhancement filtering,” in *MICCAI '98: Proceedings of the First International Conference on Medical Image Computing and Computer-Assisted Intervention*. London, UK: Springer-Verlag, 1998, pp. 130–137.

- 1
2
3
4
5 [7] S. Petkov, A. Romero, X. C. Suarez, P. Radeva, and C. Gatta, "Robust and accurate diaphragm border detection in cardiac
6 x-ray angiographies," in *Proceedings of the 3th STACOM, part of MICCAI*, 2012.
7
8 [8] Y. Cao and P. Wang, "An adaptive method of tracking anatomical curves in x-ray sequences," in *Proceedings of the*
9 *15th international conference on Medical Image Computing and Computer-Assisted Intervention - Volume Part I*, ser.
10 MICCAI'12. Berlin, Heidelberg: Springer-Verlag, 2012, pp. 173–180.
11
12 [9] Y. Zhu, S. Prummer, P. Wang, T. Chen, D. Comaniciu, and M. Ostermeier, "Dynamic layer separation for coronary dsa and
13 enhancement in fluoroscopic sequences," in *Proceedings of the 12th International Conference on Medical Image Computing*
14 *and Computer-Assisted Intervention: Part II*, ser. MICCAI '09. Berlin, Heidelberg: Springer-Verlag, 2009, pp. 877–884.
15
16 [10] C. H. Anderson, J. R. Bergen, P. J. Burt, and J. M. Ogden, "Pyramid methods in image processing," 1984.
17
18 [11] T. Lindeberg, "Principle for automatic scale selection," RIT, Tech. Rep., 1998.
19
20 [12] C. M. Bishop, *Pattern Recognition and Machine Learning (Information Science and Statistics)*. Secaucus, NJ, USA:
21 Springer-Verlag New York, Inc., 2006.
22
23 [13] E. Meijering, W. Niessen, and M. Viergever, "Retrospective motion correction in digital subtraction angiography: a review,"
24 *Medical Imaging, IEEE Transactions on*, vol. 18, no. 1, pp. 2–21, 1999.
25
26 [14] T. Meaney, M. Weinstein, E. Buonocore, W. Pavlicek, G. Borkowski, J. Gallagher, and et al., "Digital subtraction
27 angiography of the human cardiovascular system." *AJR Am J Roentgenol*, vol. 135, no. 6, pp. 1153–60, 1980.
28
29 [15] A. W. van 't Hof, A. Liem, H. Suryapranata, J. C. Hoorntje, M. J. de Boer, and F. Zijlstra, "Angiographic assessment
30 of myocardial reperfusion in patients treated with primary angioplasty for acute myocardial infarction: myocardial blush
31 grade. zwolle myocardial infarction study group," *Circulation*, vol. 97, no. 23, pp. 2302–2306, Jun 1998.
32
33
34
35
36
37
38
39
40
41
42
43
44
45
46
47
48
49
50
51
52
53
54
55
56
57
58
59
60
61
62
63
64
65